CHAPTER 7

Observation of large magnetoresistance (LMR) and quantum oscillations in $Nb_{1-x}Ta_xP$ (x=0, 0.5, 1) Weyl semimetals

Chapter 7

7.1 Introduction

Weyl semimetal (WSM) is a compound that has been considered as 3D analogous of Graphene, host low energy excitations known as Weyl fermions. It is a new class of material in which 3D Dirac cone splits into two separated Weyl cones with opposite chirality due to breaking of either time reversal symmetry (TRS) or inversion symmetry (IS) [34], [209]. When the degeneracy is lifted by violation of either TRS or IS or both some band touching points may stay gapless in WSM. These band touching points are known as the Weyl nodes and manifest linear energy dispersions along all three-dimensional (3D) momenta (k) starting from these points. A WSM surface owns the surface states in the form of metallic Fermi arc. These metallic Fermi arc surface states are associated with the bulk electronic wave functions of the material and protected by a topological invariant [210], [211].

In the electronic band structure, the Fermi arc terminates at Weyl nodes, which ignites extraordinary properties such as negative longitudinal magnetoresistance [212], chiral magnetic effects [213], anomalous Hall effect, etc [214], [215]. The first WSM phase has been experimentally observed in TaAs single crystal with a lack of inversion symmetry and nonsymmorphic space group $I4_1md$ [216]. Furthermore, a very large magnetoresistance (MR) and very high mobility has also been observed in TaAs with application of magnetic field at low temperature [217]. Similar results have also been observed in NbAs, TaP and NbP WSMs [41], [218]–[220]. Mostly, a large MR is observed in magnetic materials and is used in magnetic memory [221], in hard drives [222], and as magnetic sensors [223]. WSM gives another hope to realize extraordinarily large MR and better application results because of the extremely high mobility of charge carriers [41], [218]–[220]. Furthermore,

the helical Weyl fermions in WSM material are well protected from impurity scattering due to real spin conservation associated with the chiral Weyl nodes. Therefore, finding more WSM materials and analyzing their transport properties are very interesting for practical applications as well as for their fundamental physics. The topological categorization of metallic compounds is a consequence of Berry curvature in momentum space. In WSMs, the Weyl nodes are alike to monopoles of Berry curvature that compose the sources and sinks of Berry flux [224], [225]. Topological non-triviality of energy bands is assigned to a non-zero π-Berry phase, while a zero Berry phase is an outcome of topologically trivial energy bands. The experimental value of Berry phase can be evaluated with the help of Shubnikov-de Haas (SdH) oscillations after plotting Landau level (LL) fan diagram. Unusual MR in WSMs and its dependence on chiral anomaly can be explained from SdH oscillations analysis [226].

In this chapter, we investigated magnetotransport properties of WSM single crystal samples which were synthesized by chemical vapor transport (CVT) techniques. Form the quantum oscillation analysis we also affirmed a non-triviality of energy bands with non-zero π-Berry phase in all the samples, which confirms the presence of Weyl fermions enclosing a Weyl node in all compounds. We also report role of spin-orbit coupling (SOC) on their physical properties by electronic band structure calculations on these materials.

7.2 Experimental details

The single crystal samples of NbP, $Nb_{0.5}Ta_{0.5}P$ and TaP were grown in two step process by adhering CVT technique [43]. In first step, we have kept Nb/Ta (99.99% Alfa-Aesar) and P (99.99% Alfa-Aesar) in stoichiometric amount in vacuum sealed quartz ampoule at 950 ^{o}C inside furnace for a week, and then furnace cooled slowly to the room temperature.

In second step, after examining the phase purity of prepared polycrystalline samples by powder X-ray diffraction (XRD), all the polycrystalline samples were again vacuum sealed in quartz tube with loading of iodine (13 mg/cm^3) as a transporting agent. All the quartz tubes were again placed in a two zone furnace with creating a temperature gradient by maintaining one zone at 1050 ^{o}C (sink) and other zone at 950 ^{o}C (source) for three weeks. Finally, we obtained large polyhedral crystals with dimensions up to 1.0 mm in size, as displayed in inset of figure 7.1 (a). After grinding the pieces of obtained single crystals, the tetragonal crystal structure has been confirmed from rietveld refinement of power XRD for all grown samples, depicted in figure 7.1 (b). All transport measurements were carried out with the help of a Quantum Design physical property measurement system (PPMS).

The NbP, $Nb_{0.5}Ta_{0.5}P$ and TaP compounds were crystalized in tetragonal lattice with space group *I4$_1$md* and lattice parameters a = b = 3.333 Å, c = 11.377 Å, a = b = 3.333 Å, c = 11.374 Å and a = b = 3.324 Å, c = 11.357 Å, respectively, All the obtained lattice parameters are well matched with the previously reported work [43], [216], [226].

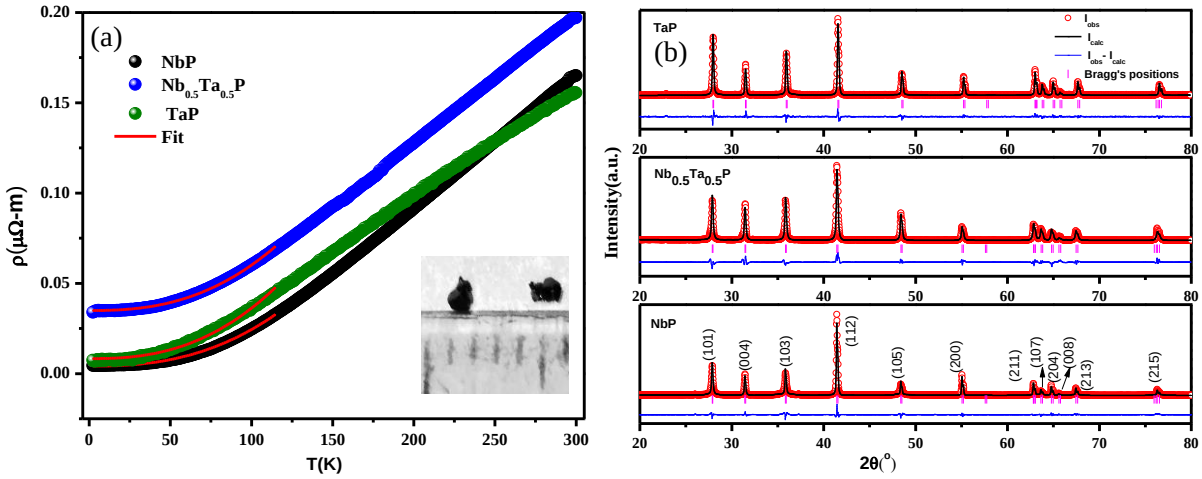

Figure 7.1: (a) Resistivity variation with respect to temperature for NbP (Black), TaP (Green) and $Nb_{0.5}Ta_{0.5}P$ (Blue) fitted with power law (Red), Inset: optical image of single crystals (b) Rietveld refinement of power XRD for all grown single crystal samples.

7.3 Computational details

For all the systems under study, electronic structure calculations were calculated by using the density functional theory based simulation package of full potential linear augmented plane wave (FP-LAPW) method implemented into WIEN2k code [227]. For the exchange correlation potential, we have adopted the well-known Generalized Gradient Approximation (GGA) proposed by Perdew, Burke, and Ernzerof (PBE)[161]. Experimental lattice parameters were used to self-consistency field (SCF) calculations and the Wyckoff positions for Nb, Ta, and P corresponding to the space group $I4_1md$ were used. The k-mesh size of 15*15*15 was set for SCF calculations, and 20*20*20 was used for an accurate electronic density of states estimation. The convergence criteria were set to be 10^{-4} Ry electronic charge/cell for the SCF calculations. The value of $R_{MT}K_{max,} = 7$ was used, which represents the plane wave cutoff parameters for the convergence criteria, where R_{MT} is smallest muffin-tin radii, and K_{max} is plane wave cutoff. The muffin tin radii for each element were set automatically such that the minimum interstitial region without overlapping the maximum occupied space by atomic spherical potential region is obtained. For the band structure plots, the number of *k*-points along the high-symmetric points corresponding to $I4_1md$ space group in the irreducible Brillouin zone was set to 1000. The effect of spin-orbital coupling on electronic structure was also incorporated to calculate the band structure for knowing the relativistic effect on bands features near chemical potential.

7.4 Results and Discussion

7.4.1 Experimental Results

The temperature dependent resistivity, ρ(T), of as-grown single crystal samples is shown in figure 7.1 (a), ρ(T) at zero applied field shows metallic nature in full measured

temperature range. The low-temperature resistivity data for all three samples (< 115 K) can be well fitted with the power law $\rho(T) = A_o + B_o T^n$ (with n ~ 2.5), where A_o and B_o are constants. The deviation from Bloch T^5 suggests correlated nature of the compounds, whereas the deviation from n=2 suggests the drift from the pure-electron-correlation-dominated scattering mechanism [228]. In high temperature range (115-300 K), linear variation of resistivity with temperature indicates dominance of electron-phonon scattering.

We have performed transfer MR measurement, i.e. MR under transfer magnetic and electric field, for all the single crystal samples. The measured MR ratio $\left[\frac{\rho_{xx}(B)-\rho_{xx}(0)}{\rho_{xx}(0)}\right] \times 100\%$, where $\rho_{xx}(B)$ is the resistivity as a function of applied magnetic field (B) and $\rho_{xx}(0)$ is the resistivity at zero field for each given temperature, is shown in figure 7.2 (a) for NbP, in figure 7.4 (a) for $Nb_{0.5}Ta_{0.5}P$ and in figure 7.6 (a) for TaP, respectively. The MR value reaches 4.1 x 10^4% for NbP, 3.65 x 10^4% for TaP and 6.7x10^3% for $Nb_{0.5}Ta_{0.5}P$ at 2 K without any sign of saturation similar to previously reported for NbP and TaP [219], [225] . Similarly, at 300 K no sign of saturation in MR value is observed for all three samples, the highest MR (153%) is observed for $Nb_{0.5}Ta_{0.5}P$ at 300 K and 7 T field, which is ~30% greater than that observed for NbP and TaP at 300 K and 7 T field. The role of scattering on MR can be understood by Kohler's scaling on MR data. The Kohler's rule [229] is given as $MR = F (B/\rho_{xx}(0))^m$, where F and m are constant. The charge carriers could show different scattering rate according to their velocities and effective mass in semimetal. Kohler predicted that if charge carriers exhibit same scattering rate then the plot between MR Vs $B/\rho_{xx}(0)$ at different temperature should merge onto a single line. It can be seen from figure 7.3 (a), 7.5 (a) and 7.7 (a) that all the MR curve below 100 K are collapse onto a single line whereas the deviation in MR data at 200 K and 300 K from this line could be associated to

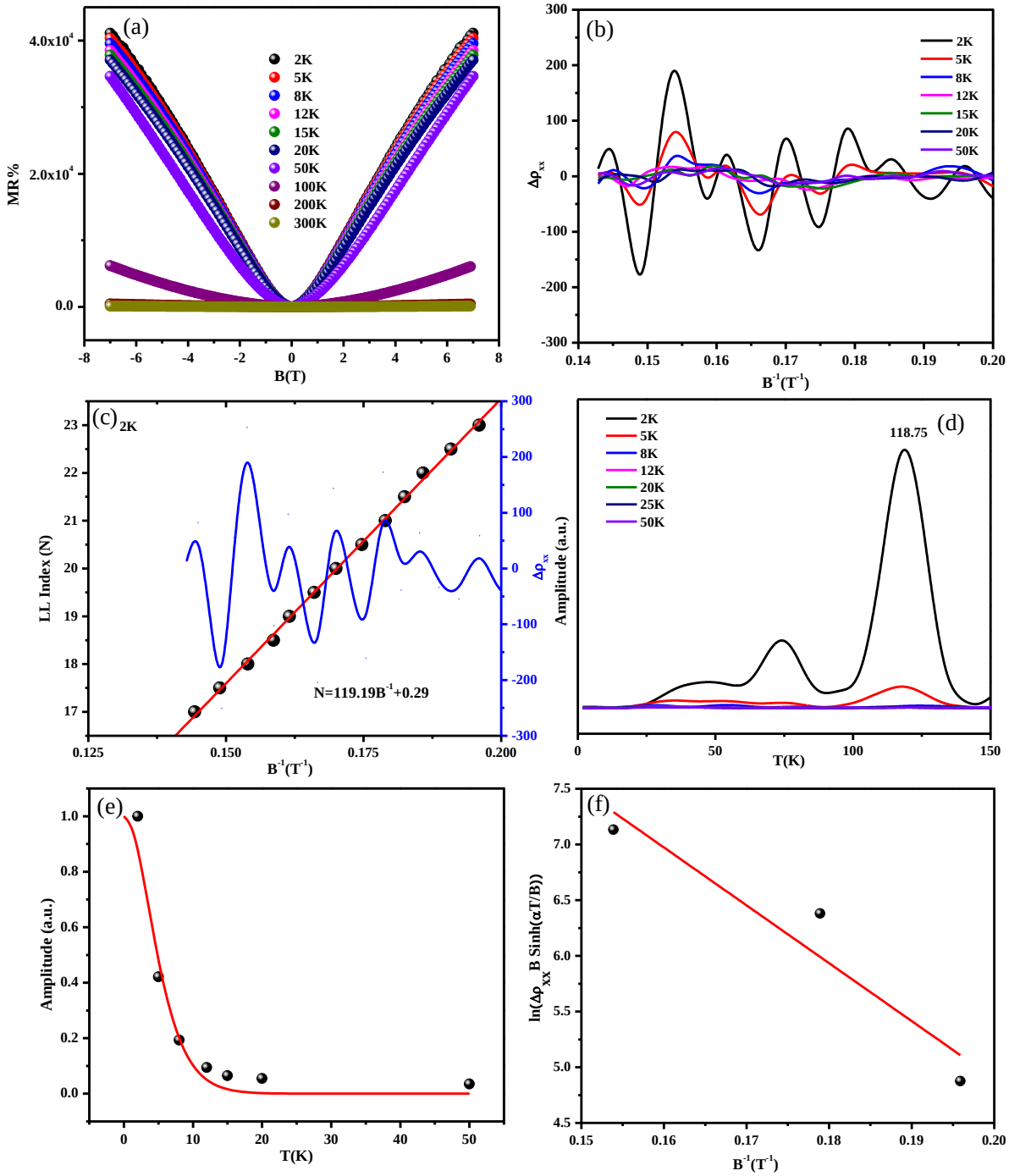

Figure 7.2: (a) The variation of MR% as a function of magnetic field at different temperatures (b) SdH oscillations at various temperatures (c) Landau levels fan diagram at 2 K (d) FFT corresponds to SdH oscillations (e) Lifshitz-Kosevich (LK) fitting on temperature dependent amplitude of the SdH oscillation at 6.498 T field and (f) Dingle damping plot with respect to inverse magnetic field for NbP compound.

phonon scattering at higher temperature. A large mobility usually gives large MR. From the Hall coefficient (R_H), the carrier concentration and carrier mobility can be calculated.

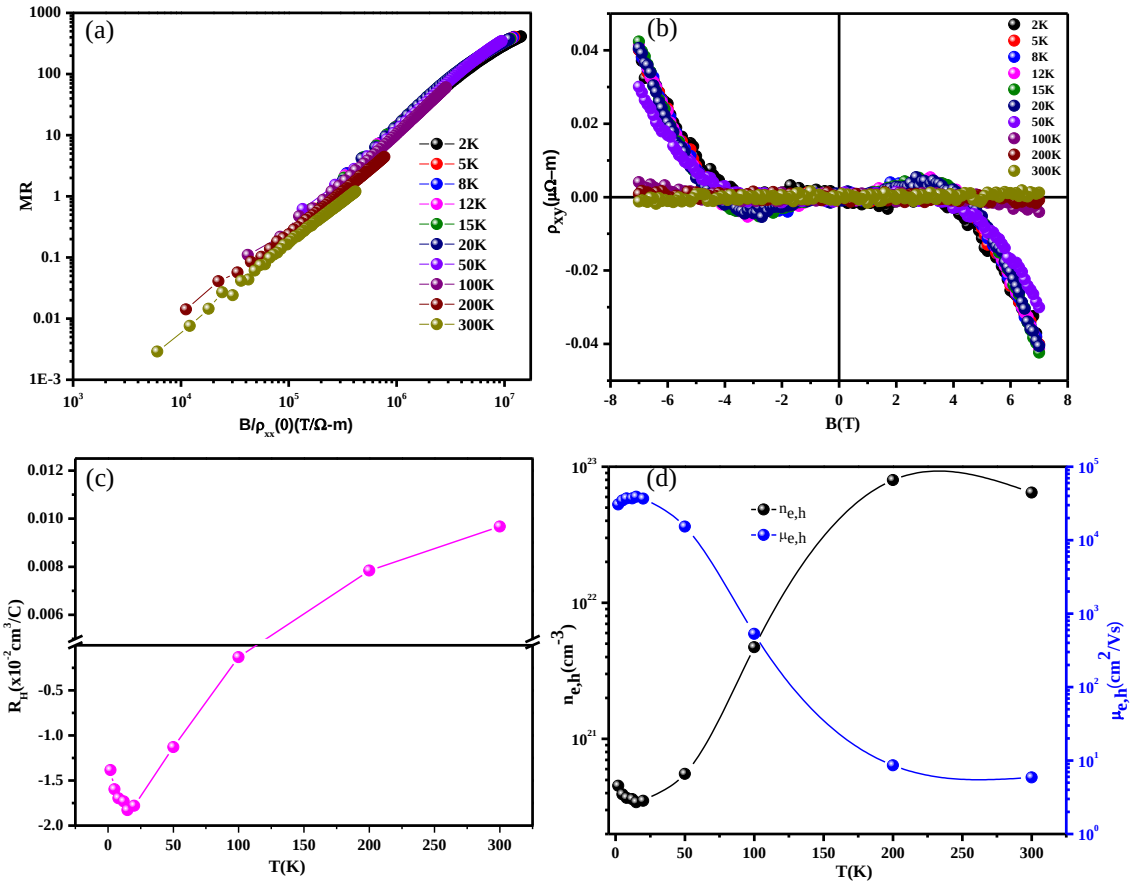

Figure 7.3: (a) Kohler's plot at different temperatures (b) Variation of Hall resistivity with respect to magnetic field at various temperatures (c) Temperature dependence of Hall coefficient and (d) The variation of carrier density and mobility of charge carrier as a function of temperature for NbP compound.

Hence, we have performed Hall measurement as a function of magnetic field at different temperatures. At the high field, the Hall resistivity $\rho_{xy}(B)$ shows a linear field dependency. However, at low field, the nonlinear behavior of $\rho_{xy}(B)$ suggests the participation of two type of charge carriers in the transport properties. Figure 7.3 (c), 7.5 (c) and 7.7 (c) display the variation of Hall coefficient R_H (T) with temperature for all three compounds, which

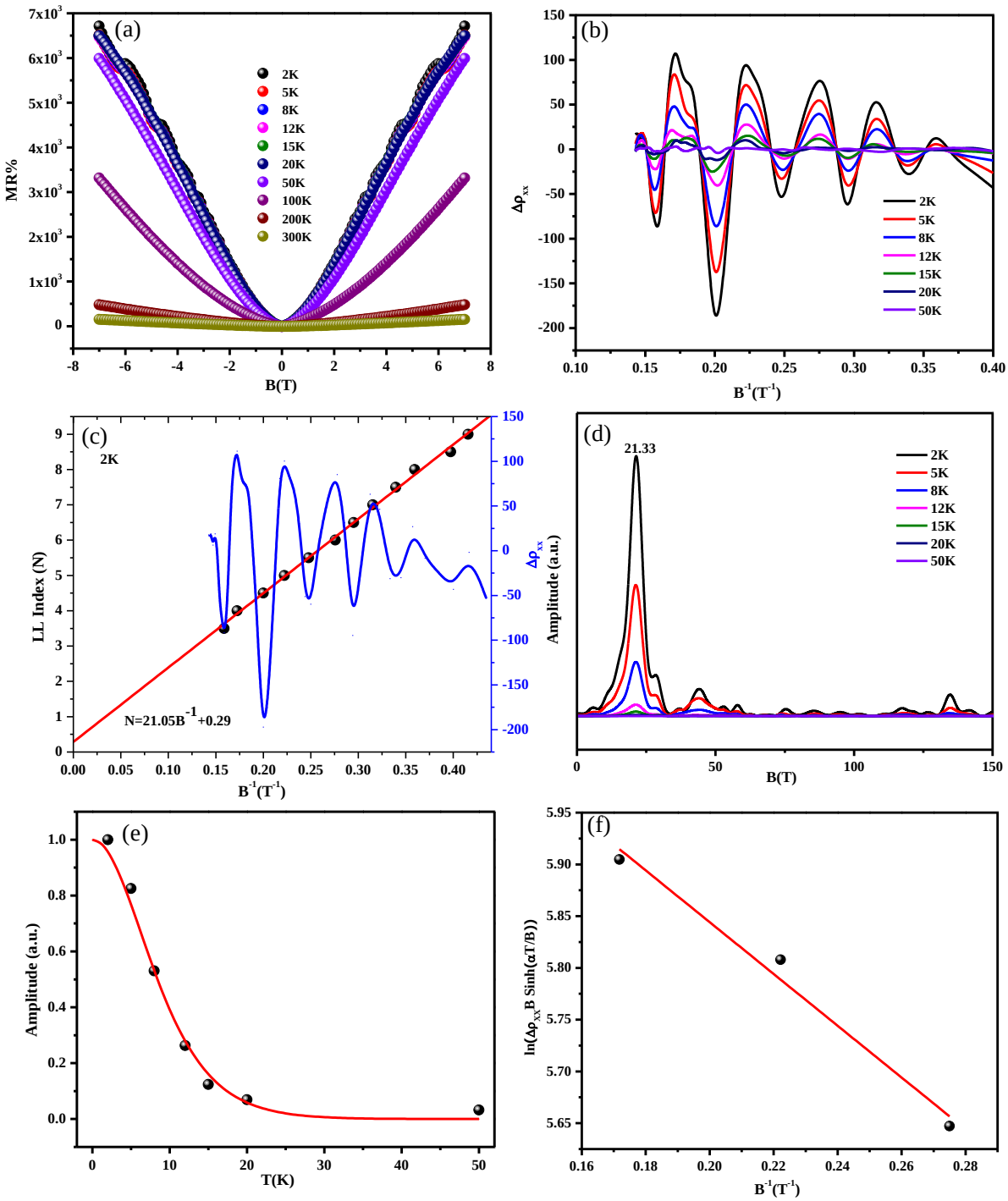

Figure 7.4: (a) The variation of MR% as a function of magnetic field at different temperatures (b) SdH oscillations at various temperatures (c) Landau levels fan diagram at 2 K (d) FFT corresponds to SdH oscillations (e) Lifshitz-Kosevich (LK) fitting on temperature dependent amplitude of the SdH oscillation at 6.341 T field and (f) Dingle damping plot with respect to inverse magnetic field for $Nb_{0.5}Ta_{0.5}P$ compound.

changes the sign from negative to positive with temperature due to the enhancement in the hole concentration at high temperature. For sake of simplicity, we have adopted single band model to evaluate the mobility and concentration of charge carriers as shown in figure 7.3 (d), 7.5 (d) and 7.7 (d). The obtained values are comparable to the values reported for Weyl semimetal compounds [219], [225].

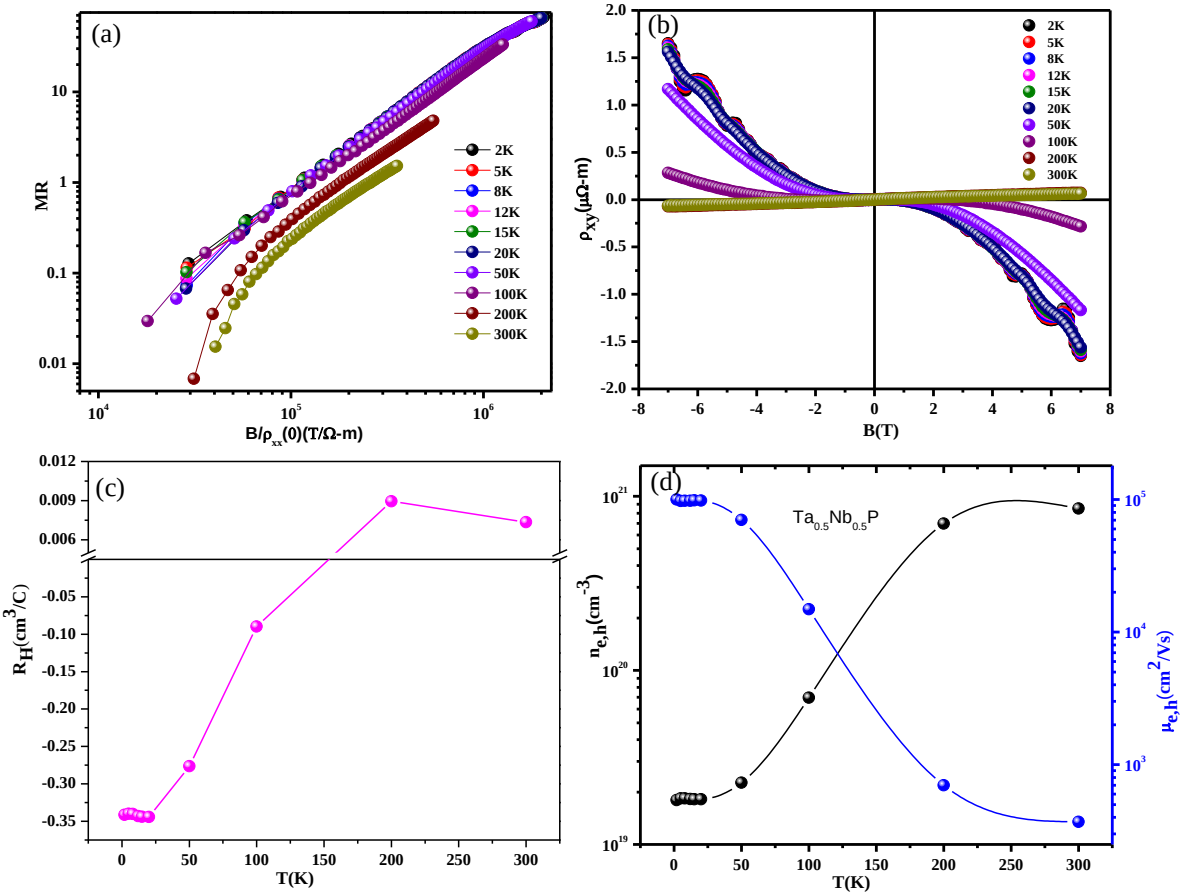

Figure 7.5: (a) Kohler's plot at different temperatures (b) Variation of Hall resistivity with respect to magnetic field at various temperatures (c) Temperature dependence of Hall coefficient and (d) The variation of carrier density and mobility of charge carrier as a function of temperature for $Nb_{0.5}Ta_{0.5}P$ compound.

In MR data, clear SdH oscillations are observed in the presence of high magnetic field at low temperature for all compounds as shown in the figure 7.2 (a), 7.4 (a) and 7.6 (a). We have extracted the SdH oscillations by subtracting a smooth background from measured MR data, and plotted it as a function of B^{-1}.

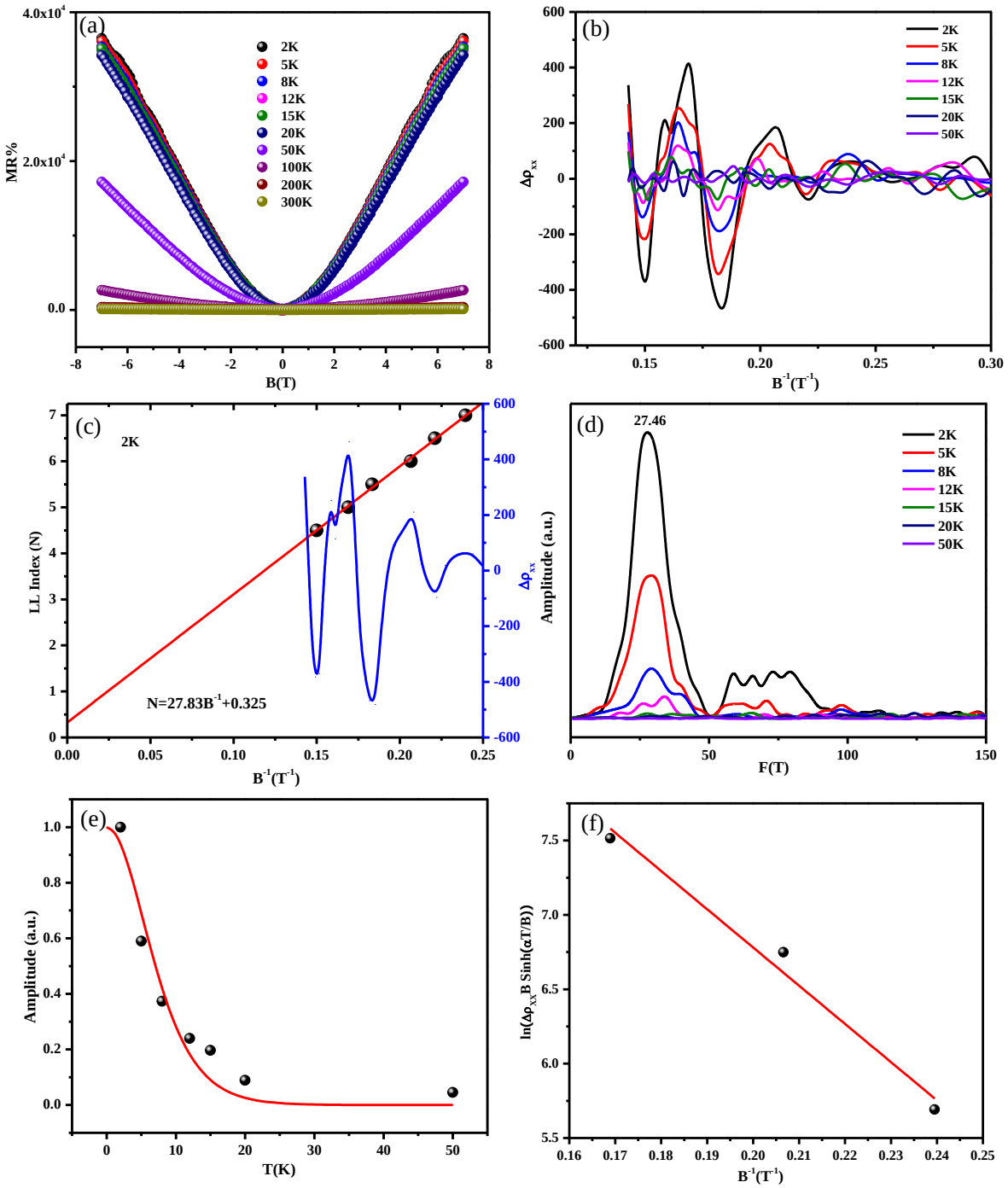

Figure 7.6: (a) The variation of MR% as a function of magnetic field at different temperatures (b) SdH oscillations at various temperatures (c) Landau levels fan diagram at 2 K (d) FFT corresponds to SdH oscillations (e) Lifshitz-Kosevich (LK) fitting on temperature dependent amplitude of the SdH oscillation at 6.665 T field and (f) Dingle damping plot with respect to inverse magnetic field for TaP compound.

The analysis of observed SdH oscillations provides the understanding of the nature of Fermi surface as well as gives the confirmation of high mobility associated to charge carriers. The observed oscillations are periodic in B^{-1}. The plots of $\Delta\rho_{xx}$ as a function of B^{-1} at different temperatures are shown in figure 7.2 (b), 7.4 (b) and 7.6 (b) and the corresponding Fast Fourier transformation (FFT) is shown in the figure 7.2 (d), 7.4 (d) and 7.6 (d). The FFT analysis of the oscillations reveals the most intense frequencies ~119T, 21 T and 27 T for NbP, $Nb_{0.5}Ta_{0.5}P$ and TaP, respectively. Furthermore, to calculate the Berry's Phase of the carriers, we have plotted Landau levels (LL) Fan diagram for all three compounds. The linear fit gives the Osanger Phase (Intercept) values 0.29, 0.29 and 0.325 for NbP, $Nb_{0.5}Ta_{0.5}P$ and TaP respectively as illustrated in figure 7.2 (c), 7.4 (c) and 7.6 (c). Strong offset of 0.29, 0.29 and 0.325 confirm the existence of Weyl fermions and nontrivial Berry's Phase for all three compounds [230], [231]. The slope of LL fan diagram gives the value of the frequency. The frequencies obtained from the slopes of LL fan diagram for all three samples are the equal to the most intense frequencies value obtained from the FFT. The Onsager relation shows the variation of the frequency with extremal cross section Fermi surface Area A_F as $F= (hA_F/4\pi^2e)$, with $A_F = \pi (k_F)^2$, where k_F is the Fermi wave vector [21]. We have evaluated the Fermi wave vectors (k_F) from Onsager relation corresponding to the different frequencies for all three compounds, the obtained values are given in the table 7.1.

We have also determined the effective cyclotron mass of charge carrier (m^*) from the temperature dependence of the oscillations which are observable up to 50 K as shown in figure 7.2 (b), 7.4 (b) and 7.6 (b). The oscillation amplitude is obtained from the different peaks of $\Delta\rho_{xx}$ for different temperatures at a constant magnetic field for all compounds, the

graphs corresponding to B=6.498 T, for NbP , B=6.341 T for $Nb_{0.5}Ta_{0.5}P$ and B=6.665 T for TaP have been shown in figure 7.2 (e), 7.4 (e) and 7.6 (e). The thermal damping factor of Lifshitz-Kosevich (LK) equation for 3D system [21], [232], $R_T = (\frac{\alpha T}{B})/\sinh(\frac{\alpha T}{B})$ has been fitted to obtain the values of m^* at above mentioned fields, where $\alpha = (\frac{2\pi^2 k_B m^*}{e\hbar})$. The obtained values m^* for all the compounds are illustrated in the table 7.1.

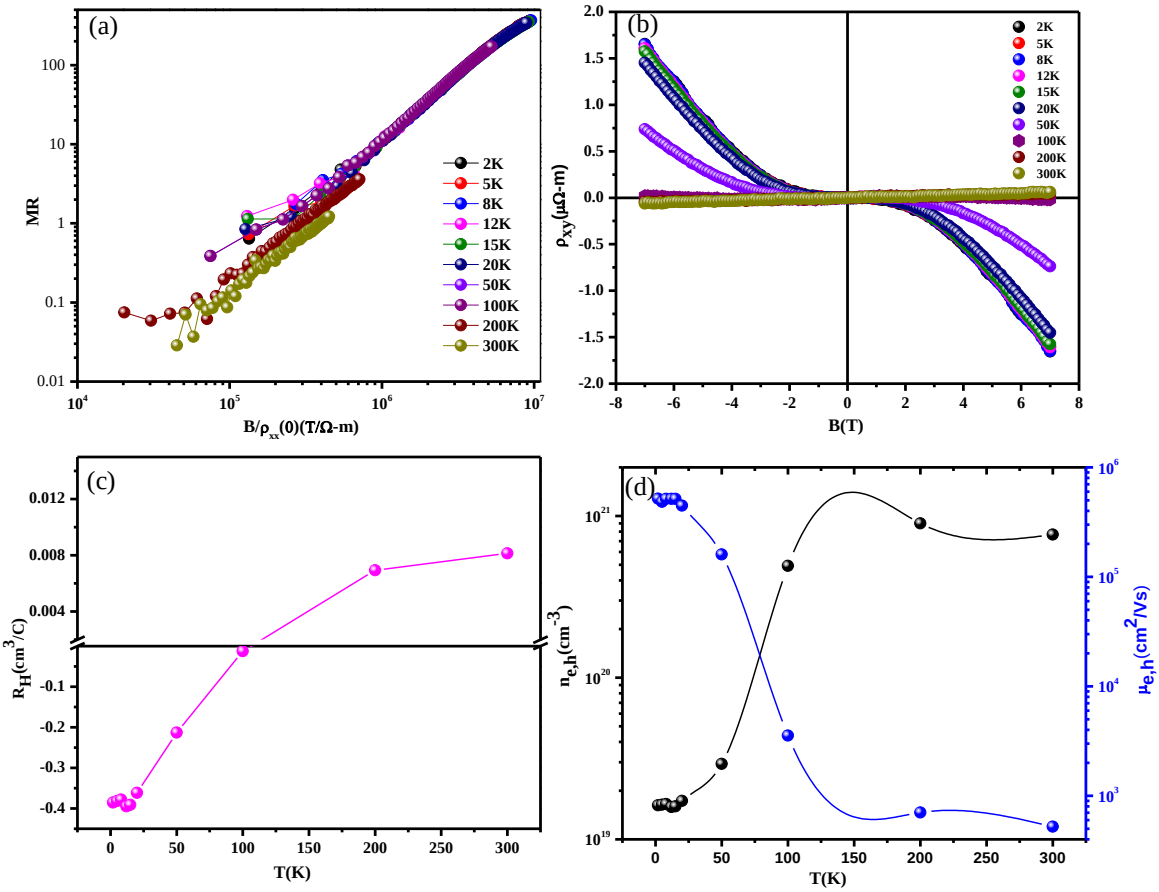

Figure 7.7: (a) Kohler's plot at different temperatures (b) Variation of Hall resistivity with respect to magnetic field at various temperatures (c) Temperature dependence of Hall coefficient and (d) The variation of carrier density and mobility of charge carrier as a function of temperature for TaP compound.

Further, by adopting the standard Dingle temperature (T_D) analysis on the Dingle damping factor $R_D = e^{-\frac{2\pi^2 k_B m^* T_D}{e\hbar B}}$, we have calculated the Dingle temperature (T_D) from

the slope of linear fit as depicted in figure 7.2 (f), 7.4 (f) and 7.6 (f). The carrier life time is calculated from $\tau = h/(4\pi^2 k_B T_D)$. Using the linear dispersion relation further we have estimated the Fermi velocity from $v_F = hk_F/2\pi m^*$. Similarly, we have also estimated the mean free path $l_{mean} = v_F\tau$, quantum mobility $\mu_q = e\tau/m^*$, and Fermi energy E_F for all the compounds, all the estimated values are indicated in the table 7.1. These physical parameters are consistent to those already reported for WSM systems [219], [225], [230], [231]. From the table it can be seen that intermediate compounds shows low dingle temperature, large carrier life time, mean free path and large quantum mobility due to small scattering of the charge carrier in the presence of magnetic field as well as small effective cyclotron mass as compared to end compounds. The diminish in the MR for $Nb_{0.5}Ta_{0.5}P$ as compared to end compounds is might be due to small scattering of the charge carriers in the presence of magnetic field and low carrier concentration. Therefore, results are indicating that $Nb_{0.5}Ta_{0.5}P$ could be a good WSM material.

7.4.2 Computational Results

The electronic structure calculations for all the systems were performed in the non-spin polarization configuration.

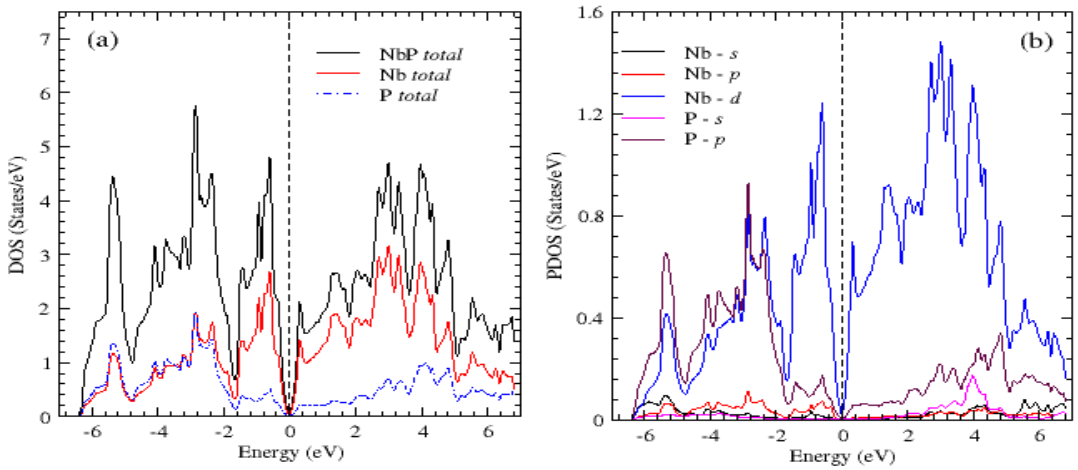

Figure 7.8: Shows (a) total density of states, and (b) partial density of states for NbP.

The calculated results of total and partial density of states for all systems are shown in figures 7.8 (NbP), 7.9 (TaP), and 7.10 ($Nb_{0.5}Ta_{0.5}P$). As it can be seen clearly from the total density of states (TDOS) plot for all the systems plotted in figure 7.8 (a), 7.9 (a), 7.10 (a), there are non-zero finite density of states at Fermi level. Such finite DOS values suggest that both parent (NbP and TaP) and mixed composition ($Nb_{0.5}Ta_{0.5}P$) systems possesses the typical semi-metallic characteristics. The feature of semi-metallic nature in $Nb_{0.5}Ta_{0.5}P$ kept remain and provide an interesting electronic structure in the vicinity of chemical potential, so that one can expect to get very fascinating physical properties from this material within Weyl semi-metal family.

The variation in TDOS below and above the Fermi level (E_F) have sharp steep like variation with larger magnitude of density of states in valance band region than that of the conduction band. The contribution in total density of states is from the wide energy region covering the 6 eV range above and below the $E_{F.}$ The values of TDOS at E_F for NbP, TaP, and $Nb_{0.5}Ta_{0.5}P$ are found to be ~0.087, 0.042, 0.067 states/eV/unit cell, respectively. Within the single parabolic band model of free electron theory, the electrical conductivity is directly related to the magnitude of the DOS at $E_{F,}$ suggesting that NbP system with high electrical conductivity whereas TaP with lowest electrical conductivity among the three systems. However, for the quantum mechanical theory of interacting electrons system possessing the Weyl semi-metallic characteristics, one need to consider beyond the consideration of the magnitude at E_F, such as the contributions in transport behavior from the spectral conductivity in the vicinity of chemical potential. The spectral conductivity is obtained from the energy derivative of DOS, thus variation in DOS is very important to analyses the electrical transport behavior. Here, among all the composition, we can clearly

see that NbP (figure 7.8 (a)) and TaP (Fig. 7.9 (a)) have almost similar magnitude of $DOS_{max} \geq 5$ states/eV/unit cell in the VB region, whereas in case of $Nb_{0.5}Ta_{0.5}P$, the DOS_{max} is $\leq$ 5states/eV/unit cell. From this observation we can expect the lowest electrical conductivity for the $Nb_{0.5}Ta_{0.5}P$ system in comparison to the parent system of NbP and TaP.

Band dispersion plots along the high-symmetric direction are very important to understand the transport behavior possesses by the Weyl fermion system. We have calculated the band dispersions for all three compositions without (shown in figures 7.11 (a), 7.12 (a), and 7.13 (a)) and with (shown in figures 7.11 (b), 7.12 (b), and 7.13 (b)) consideration of relativistic spin-orbit coupling (SOC) effects for NbP, TaP and $Nb_{0.5}Ta_{0.5}P$ system, respectively. The band dispersions are plotted along the high-symmetric directions by considering the *k*-path ϒ-N-Z-ϒ-X in the irreducible Brillouin zone.

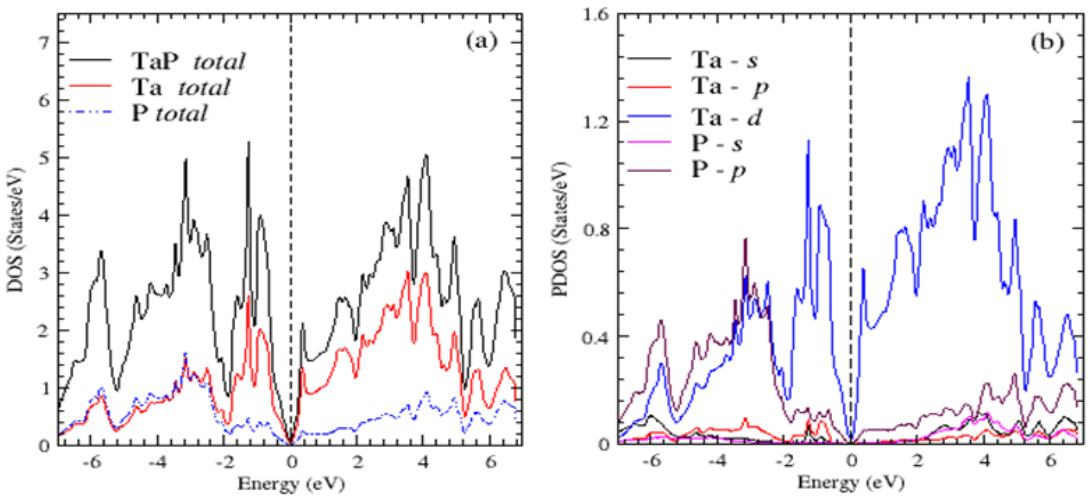

Figure 7.9: Shows (a) total density of states, and (b) partial density of states for TaP.

For all the three systems, we observe the linearly dispersive bands about chemical potential. These linear bands touch at multiple locations of k-points known as Weyl points. In addition to the non-separable bands at Weyl nodes, the bands are penetrating at different high-symmetric k-points into Fermi level clearly suggesting the semi-metallic nature of all

the systems. Without SOC, the bands are touching each other and have the doubly degenerate band. The degeneracy of the bands near Fermi level kept remains about the Weyl node points while moving along the N-Z direction. After including the SOC effect, it results into the change in band energy with separation of energy bands with each other in lifting out the degeneracy. The separation of bands occurs for both bands below and above of the Fermi level.

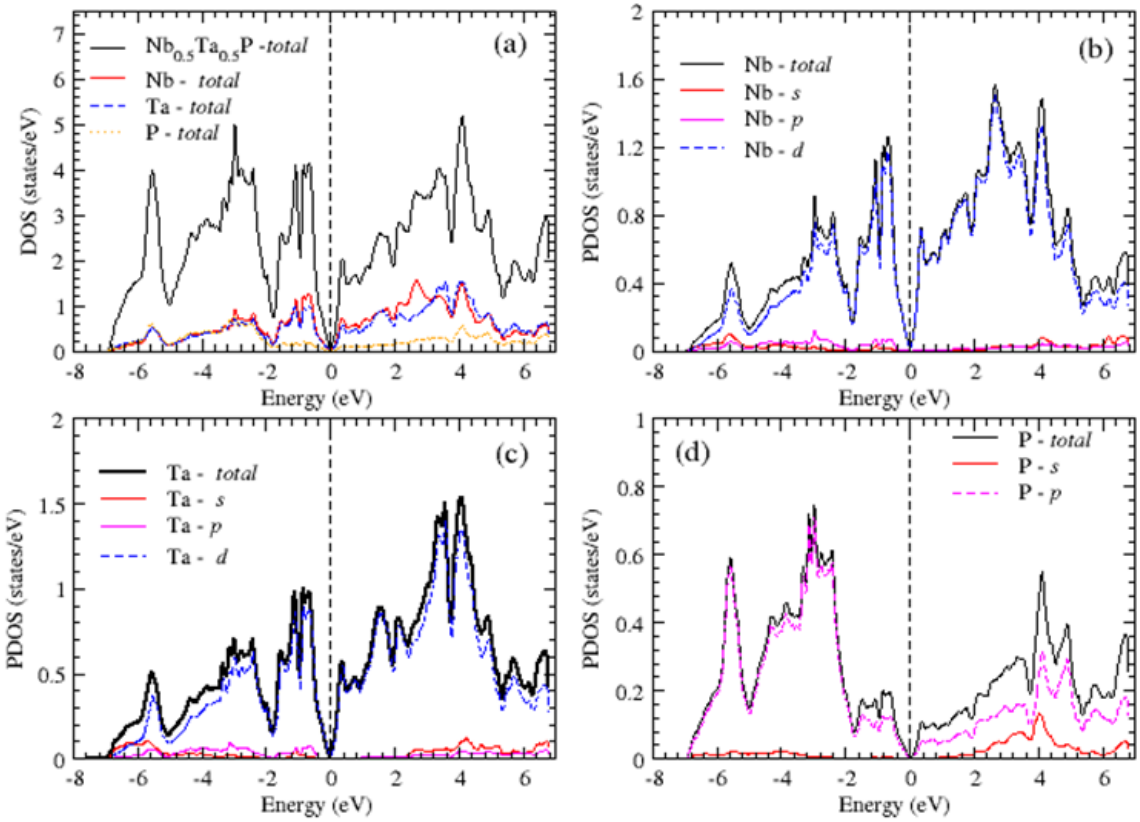

Figure 7.10: Shows (a) total density of states and (b, c, d) partial density of states for $Nb_{0.5}Ta_{0.5}P$.

In case of NbP system, although the observation of degeneracy lifts out between two Weyl points is very clear, however, the bands again become degenerate at Weyl points. The separation in the energy of bands due to SOC effect is clearly observed along N-Z direction,

while at few k-points along N-ϒ points also can be seen. Along the ϒ-X direction the SOC effects is very weak as the bands in this region are 200 meV below the Fermi level.

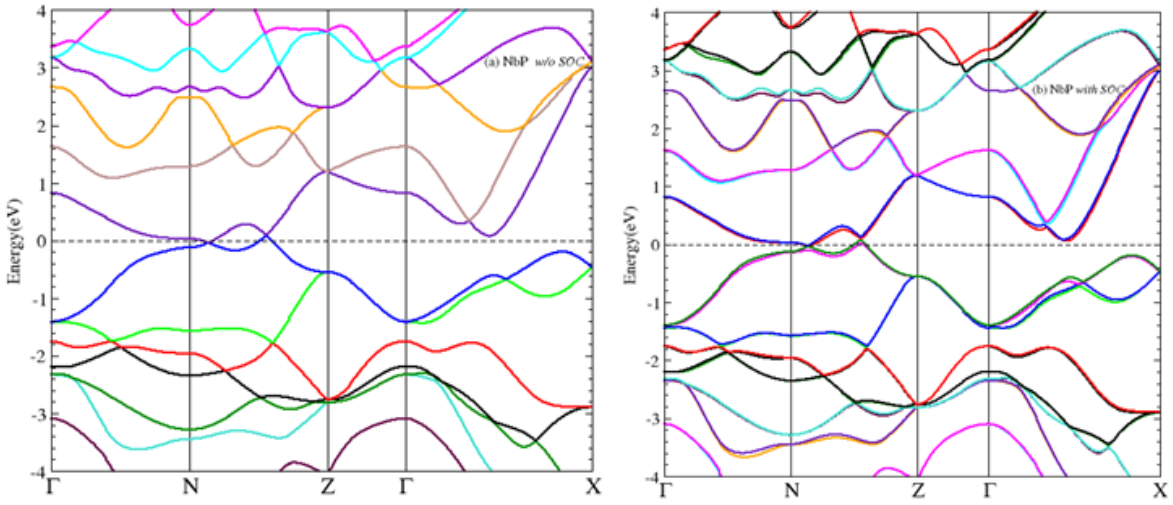

Figure 7.11: Shows band dispersion of NbP (a) without SOC, and (b) with SOC.

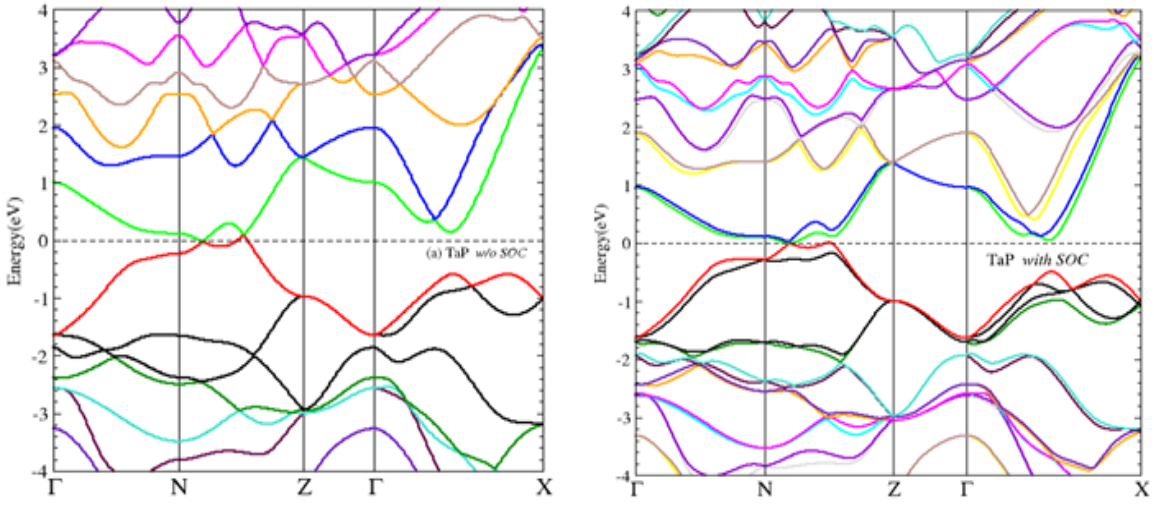

Figure 7.12: Shows band dispersion of TaP (a) without SOC, and (b) with SOC.

The similar feature of Weyl semi-metal characteristics and bands separation occurrences we observed in case of TaP systems also. Notably, in case of TaP, we clearly observe the gap opening at Weyl nodes. The bands become well separated along the multiple k-path directions with SOC effect for e.g. along direction N-Z, N-ϒ, and ϒ-X directions for the valance band region, where as for the conduction band, the band splitting

is much prominent along N-Z, and ϒ-X directions while along N-ϒ direction very weak separation occurs within the degenerate bands. Besides the gap opening at few Weyl nodes with SOC, the bands still cross in the vicinity of $E_{F,}$ and absence of clear gap opening across the Fermi level have the clear indication of semi-metallic feature of this system also.

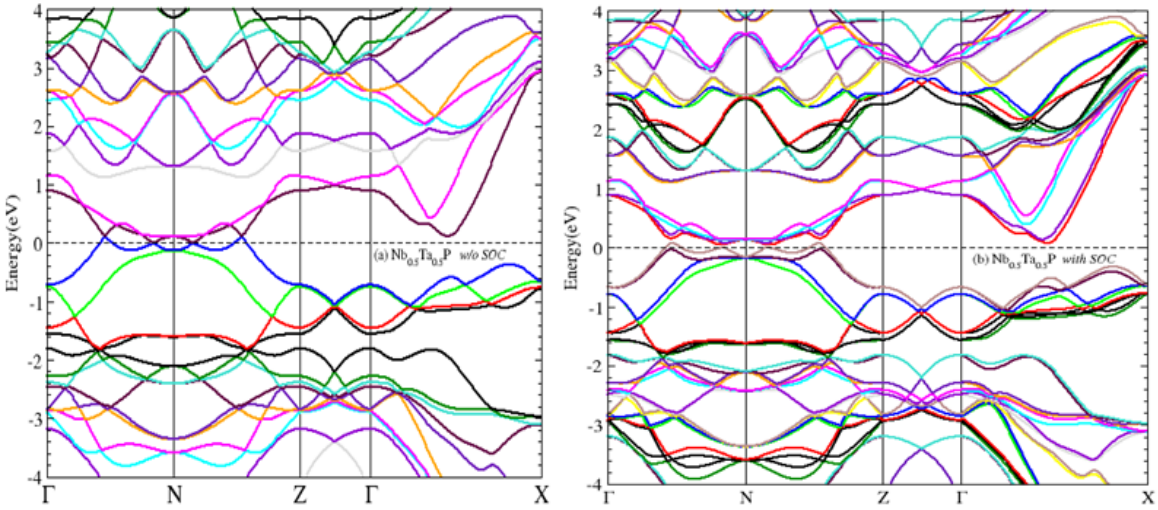

Figure 7.13: Shows band dispersion of $Nb_{0.5}Ta_{0.5}P$ (a) without SOC, and (b) with SOC.

For the $Nb_{0.5}Ta_{0.5}P$ system, the band dispersion shows the multiple Weyl nodes. Without SOC the bands are found to be crossing at multiple *k*-points with linearly dispersive characteristics. By imposing the SOC effect, the bands are found to be well separated along the *k*-path and clear cut gap is observed above the 50 meV of the Fermi level. Such band gap formation above the E_F, while having the separated band penetration from VB is typical pseudogap like feature. Therefore, safely one can consider it as semi-metallic system within the approximation used to compute the band dispersion in present study. The bands in both above and below the Fermi level gets well separated, and degeneracy is clearly lifted out at multiple Weyl nodes at band crossing is outcome result of inversion symmetry or time reversal symmetry. Both opening of gap and semi-metallic characteristics together with linear band dispersion across Weyl points make the $Nb_{0.5}Ta_{0.5}P$

system very favorable from electronic structure point of view to exhibit interesting electronic transport properties.

	NbP	$Ta_{0.5}Nb_{0.5}P$	TaP
m^*	0.1968 m_0 at B=6.498 T	0.10873 m_0 at B=6.341 T	0.1394 m_0 at B=6.665 T
T_D	17.95 K	1.54 K	12.54 K
τ	$6.77x10^{-14}$ s	$7.904x10^{-13}$ s	$9.694x10^{-14}$ s
K_F	$1.508x10^{9}$ m^{-1}	$6.338x10^{8}$ m^{-1}	$7.286x10^{8}$ m^{-1}
V_F	$8.87x10^{5}$ m/s	$6.64x10^{5}$ m/s	$6.0551x10^{5}$ m/s
l_{mean}	59.43 nm	524.56 nm	58.70 nm
μ_q	$6.05x10^{2}$ cm^2/v.s	$1.251x10^{4}$ cm^2/v.s	$1.22x10^{3}$ cm^2/v.s
E_F	880 meV	277 meV	290 meV
n_b	$1.15x10^{20}$ cm^{-3}	$8.598x10^{18}$ cm^{-3}	$1.3064x10^{19}$ cm^{-3}

Table 7.1: Various parameters evaluated from SdH oscillation analysis for all three compounds.

7.5 Conclusion

In conclusion, we have grown WSM single crystal samples by adopting chemical vapor transport (CVT) techniques. Large polyhedral crystals were obtained for all three compounds. Resistivity as a function temperature depicts a semi-metallic nature for all the samples, similar nature for all the systems is also predicated by DFT calculations. In low-temperature range (< 115 K), pure-electron-correlation-dominated scattering mechanism has been found from power-law fitting, while the dominance of electron-phonon scattering is observed in high-temperature range (115 K-300 K). Very large MR value and SdH oscillations are observed for all the compounds, this large value of MR is assigned to the large mobility of the charge carriers. The different scattering rate of charge carriers is confirmed by Kohler's scaling. The different parameters associated to the charge carriers are extracted by SdH oscillation analysis for all the systems, which confirmed the quasi-particle nature of charge carriers. Moreover, the Hall coefficient changes their sign from negative to positive around 110 K for all three compounds, suggested that all the systems

are electron-hole compensated systems. The linearly dispersive band-crossing points in the vicinity of Fermi level have been predicted from the DFT calculation for all three WSM systems. Overall, it is observed from the experimental and theoretical analysis that $Nb_{0.5}Ta_{0.5}P$ system exhibits very interesting electronic transport properties.